LA-UR-02-5054

c.1

Title: STRATUS CLOUD STRUCTURE FROM MM-RADAR TRANSECTS AND SATELLITE IMAGES: SCALING PROPERTIES AND ARTIFACT DETECTION WITH SEMI-DISCRETE WAVELET ANALYSES

Author(s): Anthony B. Davis, Nikola P. Petrov,
Space & Remote Sensing Sciences Group (NIS-2)
Eugene E. Clothiaux
Dpt. of Meteorology, The Penn State University
and Alexander Marshak
Climate & Radiation Branch, NASA - GSFC

Submitted to: On-line Proceedings of
12th Atmospheric Radiation Measurement (ARM) Program
Science Team Meeting
Saint Petersburg (Fl), April 8-12, 2002

Los Alamos
NATIONAL LABORATORY

STRATUS CLOUD STRUCTURE FROM MM-RADAR TRANSECTS AND SATELLITE IMAGES: SCALING PROPERTIES AND ARTIFACT DETECTION WITH SEMI-DISCRETE WAVELET ANALYSES

Anthony B. Davis
Space & Remote Sensing Sciences Group, Los Alamos National Laboratory
Los Alamos, NM 87545, USA.

Nikola P. Petrov
Department of Physics, The University of Texas at Austin
Austin, Tx 78712, USA.

Eugene E. Clothiaux
Department of Meteorology, The Pennsylvania State University
503 Walker Building, University Park, Pa 16802, USA.

Alexander Marshak
Climate & Radiation Branch, NASA - Goddard Space Flight Center
Greenbelt, Md 20771, USA.

Abstract

Spatial and/or temporal variabilities of clouds is of paramount importance for at least two intensely researched sub-problems in global and regional climate modeling:
- cloud-radiation interaction where correlations can trigger 3D radiative transfer effects; and
- dynamical cloud modeling where the goal is to realistically reproduce the said correlations.

We propose wavelets as a simple yet powerful way of quantifying cloud variability. More precisely, we use "semi-discrete" wavelet transforms which, at least in the present statistical applications, have advantages over both its continuous and discrete counterparts found in the bulk of the wavelet literature.

With the particular choice of normalization we adopt, the scale-dependence of the variance of the wavelet coefficients (i.e., the wavelet energy spectrum) is always a better discriminator of transition from "stationary" to "nonstationary" behavior than conventional methods based on auto-correlation analysis, second-order structure function (a.k.a. the semi-variogram), or Fourier analysis. Indeed, the classic statistics go at best from monotonically scale- or wavenumber-dependent to flat at such a transition; by contrast, the wavelet spectrum changes the sign of its derivative with respect to scale.

We apply 1D and 2D semi-discrete wavelet transforms to remote sensing data on cloud structure from two sources:
- an upward-looking milli-meter cloud radar (MMCR) at DOE's climate observation site in Oklahoma deployed as part of the Atmospheric Radiation Measurement (ARM) Program; and
- DOE's Multispectral Thermal Imager (MTI), a high-resolution space-borne instrument in sun-synchronous orbit that is described in sufficient detail for our present purposes by Weber et al. (1999).

For each type of data, we have at least one theoretical prediction —with empirical validation already in existence— for a power-law relation for wavelet statistics with respect to scale. This is what is expected in physical (i.e., finite scaling range) fractal phenomena. In particular, we find long-range correlations in cloud structure coming from the important nonstationary regime. More surprisingly, we also uncover artifacts the data that are traceable either to instrumental noise (in the satellite data) or to smoothing assumptions (in the MMCR data processing). Finally, we discuss the potentially

damaging ramifications the smoothing artifact can have on both cloud-radiation and cloud-modeling studies using MMCR data.

Background on Wavelet Transforms and Scaling Laws

The wavelet transform of a signal $f(x)$ is essentially a convolution with a scaled replicate of an oscillating function $\psi(x)$:

$$T_\psi[f](a,b) = a^{-1} \int f(x)\, \psi(\,(x-b)/a\,)\, dx. \qquad (1)$$

where x is real for a time-series and a 2D vector for an image. (We use the vector notation here for more generality.) The arguments (a,b) are respectively the scale and position of the wavelet $\psi(\cdot)$. Figure 1 shows the popular Haar wavelet which is piece-wise constant in both 1D and 2D. In the latter case, there are in fact 3 possible wavelets associated with differences the horizontal and vertical directions and across diagonals.

We will be seeking scaling relations for the wavelet coefficients in Eq. (1), i.e., a parametric representation of

$$\langle T_\psi[f](a,b)^2 \rangle_b \sim a^{2H}, \qquad (2)$$

where $\langle \cdots \rangle_b$ means averaging over the argument b. This is simply the variance of $T_\psi[f](a,b)$ as long as $\langle T_\psi[f](a,b) \rangle_b = 0$ which means that there is no overall trend in the data, assuming $\psi(x)$ has single oscillation (per direction in 2D). For better accuracy, the wavelet coefficients in Eq. (1) are ordered by increasing value before summing their squares at each scale $a \geq \ell$, the pixel scale. The exponent H in Eq. (2) is then obtained by linear regression in log-log axes.

Following Arnéodo et al. (1995), we note that using $\psi_{SF}(x) = \delta(x-\ell) - \delta(x)$ in Eq. (1) for 1D brings us back to the classic structure functions, of turbulence theory fame in particular. The parameter H in Eq. (2) is a Hurst-like exponent that has the usual (Mandelbrot 1982) meaning when between 0 and 1, as expected in the vast literature using $\psi_{SF}(x)$. When using more interesting wavelets, H can, in principle, be negative or greater than unity depending on the choices of f and ψ. For instance, with the non-standard normalization used in (1), δ-correlated stationary (or "white") noise yields $H = -1/2$. By the same token, exactly "$1/f$" noise yields $H = 0$ while smooth (everywhere differentiable) signals yield $H = 1$. Consider the following examples:

- Stationary behavior is found in uncorrelated instrumental noise at very small scales and after the large-scale decorrelation of cloudiness; here, wavelet coefficients decrease with increasing scale.
- Nonstationary behavior is found in the turbulence of horizontal structure in clouds as well as instrumental or physical smoothing in the data; here, wavelet coefficients increase with scale.

Figure 2c illustrates these trends in the wavelet spectrum schematically while panels 2a and 2b show the corresponding outcomes of Fourier and structure-function analyses respectively. The reason the wavelets are scaled as prescribed in (1) is now clear. The exponents of the statistical moments of the coefficients are the same as for structure functions at all orders, at least for nonstationary signals with stationary increments.

FIGURE 1 here

Figure 1: *Haar wavelets and scaling functions in 1D* (left) *and in 2D* (right). The top row are the scaling functions, followed by the characteristically piece-wise constant wavelets.

FIGURE 2 here

Figure 2: *Variability analysis in an idealized turbulence experiment.* The "integral" scale R marks the transition from the inertial sub-range, where presumably a down-scale Kolmogorov cascade is unfolding, to an independent cascade. The Kolmogorov or "dissipation" scale η marks the transition from inertial- to dissipation-dominated dynamics. We assume here that the sampling is such that instrumental (e.g., velocity probe) noise dominates the smallest scales, hence a final scale break without any physical significance. **(a)** Fourier spectrum. **(b)** Structure functions. **(c)** Wavelet variance/energy spectrum.

Discrete and Semi-Discrete Wavelet Transforms

In the wavelet literature, the integral transform in (1) is assumed continuous in a and b; it is also very redundant. Complete removal this redundancy is achieved by the discrete wavelet transform where

$$a_j = 2^j \times \ell, \tag{3}$$

where $j = 0, ..., j_{max}$ while b is sampled on a grid of constant $2a_j$. This enables Mallat's (1989) efficient cascade technique for computing $T_\psi[f](a,b)$ known as "multi-resolution analysis" or MRA. The maximum scale of interest is determined by j_{max} which is set to the integer part of $\log_2 N - 1$ where N is the length of the times series in 1D, or to that of $\log_2 \min\{N_x, N_y\} - 1$ for a 2D field or "image" with $N = N_x \times N_y$ pixels. The algorithmic complexity of an MRA is N, as illustrated on a simple example in Fig. 3.

We prefer to use the "semi-discrete" wavelet transforms which are discrete in scale, but continuous in position (Davis et al. 1999, and references therein): b covers all *possible* positions. That means all positions where the support of the wavelet is still inside the data field. The number of coefficients and algorithmic complexity then grows only as $N\log N$, where N is the number of points (pixels) in the time-series (image). The redundancy of this representation at each scale has been exploited previously, using several different terminologies which would be misleading here, in denoising and data compression applications but we see it as a safeguard when cumulating spatial statistics. Notice that, by now, we have effectively relaxed the habitual (Daubechies 1992) constraints of orthogonality and normalization in discrete wavelet theory.

The semi-discrete wavelet transform was implemented using a simple variant of Mallat's (1989) MRA trick which calls for recursive estimation of the coefficient of "scaling function" $\varphi(x)$ associated with the Haar wavelet (or wavelet family in the 2D case). This is simply the average over 2 neighboring pixels at any scale (4 in the 2D case). For more details, we refer to Davis et al. (1999). For better memory management (especially in 2D), this averages in Eq. (2) are computed during the multi-resolution recursion at a given a_j in (3).

FIGURE 3 here

Figure 3: *Discrete Haar wavelet analysis in 1D using multi-resolution analysis for $N = 16$.* The alternate notation $<\psi_{a,b},f>$ for $T_\psi[f](a,b)$ in Eq. (1) is used here where $\psi_{a,b}(x) = \psi((x-b)/a)$. At each step in the (inverse) cascade, *disjoint* 2-pixel averages are computed, yielding the scaling-function coefficients. They are only used to proceed to the next (larger) scale. In the semi-discrete wavelet transform, the only difference is that the 2-pixel averages are not disjoint but, on the contrary, sampled continuously (i.e., at the smallest pixel scale ℓ).

1D Horizontal Transects of mm-Radar Reflectivity

We first analyze a 6-day long sequence of cloud mm-radar data collected at the ARM Southern Great Plains site, January 9–14, 1998. Vertical profiles of reflectivity $Z_t(z)$ are re-mapped into constant altitude transects $f_z(x) \equiv Z_t(z)$, where $x = vt$ (v being the appropriate advection velocity). A full suite of range bins with $\Delta z = 45$ m is captured every $\Delta t = 10$ s (hence $\Delta x \approx 50$ m at a nominal ≈ 5 m/s advection speed). The data displayed in Fig. 4 are not very interesting to visualize. Indeed, during this long cloudy episode, there was always a low-level cloud occupying typically the first 20 levels, and not much else. We performed 1D semi-discrete wavelet analyses for each level, using 5 short instances of linear interpolation to compensate for the data drop-out between 24-hour periods.

Figure 5 shows a log-log plot of $\log_2 \langle T_\psi[f](a,b)^2 \rangle_b$ versus $j = \log_2(a/\Delta x) = \log_2 a + constant$ from Eq. (3) for levels $z = 180$ m and 630 m. The range of scales is huge, from 10 s to 10×2^{14} s, which is ≈ 46 hours (corresponding to several hundred km).

We see that the lower layers exhibit three scaling regimes. As scale increases, we see a very smooth regime, with H close to 1, followed by a regime with $H \approx 1/3$ which is characteristic of boundary-layer turbulence, and finally we see a stationary regime with $H < 0$. Keeping the mean wind constant at ≈ 5 m/s, transitions are respectively at ≈ 0.5 km and ≈ 50 km. The latter scale is probably somewhat exaggerated since the wind eventually meanders.

The small-scale transition from turbulence to smoothness is not observed in any in-situ probings that we know of. In fact, it is perfectly well explained by the interpolation performed between 4 or more neighboring horizontal samples in the specific "best estimate" radar operation mode used here. As it turns out, this mode is designed for whole-column monitoring and compromises the sampling in the boundary layer. The interpolation remedy is safe in the sense of mean values but it corrupts the correlation structures.

As an example, it would be very misleading to use these radar data at small scales to assess cloud model performance (e.g., using a Large-Eddy Simulation or LES) since, in dynamical modeling too, it is unfortunately necessary to introduce an artificial smoothing. In this context, the artificial smoothing is used to control small-scale numerical instabilities. A MMCR-to-LES comparison would be a reasonable approach to model validation. However, it will lead to the erroneous conclusion that the numerical smoothing procedure has a minimal impact on the model output since cloud structure is *apparently* smooth at the smallest observable scales.

Another source of confusion can follow by comparing the interpolated MMCR field with high-resolution satellite (e.g., LANDSAT) images at visible/near-IR wavelengths which are affected inherently by radiative smoothing. This is an inescapable physical process due to the multiple scattering. It explains in particular the observed decoupling of spatial fluctuations in zenith radiance and in liquid water path at scales smaller than about the cloud thickness (Davis et al. 1997), precisely a few hundred meters in the present case. Here, a MMCR-to-LANDSAT comparison would lead to the erroneous conclusion that the radiative smoothing is either absent or has a minimal effect on already smooth small-scale cloud structure.

We strongly recommend that either the temporal radar sampling be increased so that the interpolation becomes unnecessary or that the reflectivity profiles be archived at a resolution which is dynamically as well as radiatively meaningful.

In contrast, the large-scale transition is apparently real and probably related to the scale-breaks observed in reflected (Austin et al. 1999) and transmitted (Savigny et al. 2002) radiance fields at several tens of kilometers. The likely micro-physical explanation for this scale-break is the

cap imposed on liquid water path, hence its variability, in stratus layers by the onset of efficient drizzle production. This process is still poorly understood.

The higher layers exhibit just two scaling regimes: the same artificially smoothed regime as for the low levels, and a long essentially flat regime (for the wavelet coefficient). This corresponds to a "1/f" spectrum, the very same scaling that has been observed in recent meso-scale satellite studies for TOA temperature fluctuations (J.-I. Yano, private communication). The change in scaling with height emphasizes the statistical anisotropy and heterogeneity of cloudiness.

FIGURE 4 here

Figure 4: *MMCR data from the SGP site for January 9–14, 1998.* The standard (Clothiaux et al. 1995) rendering of "best-estimate" radar reflectivity is used along with the cielometer-based lower cloud boundary. Time increases day-by-day from left to right, then top to bottom.

FIGURE 5 here

Figure 5: *1D semi-discrete wavelet spectrum analysis of horizontal layers of ARM cloud-radar data in Fig. 4.* Solid line: z =180 m; dashed line: z = 630 m.

2D Correlations in a Solar-Channel Cloud Scene from the Multispectral Thermal Imager

We now turn to data from MTI, a high-resolution push-broom imaging spectro-radiometer with state-of-the-art calibration (especially in the thermal IR channels). In the visible/near-IR spectral region of interest here, the pixels have a mere 5 m footprint (better resolution is now commercially available, but only in pan-chromatic mode). We investigated a completely cloud-covered scene of opportunity which is very smooth across the whole image. MTI's focal plane has three sensor chip arrays (SCAs) that build up the complete swath. The most striking feature of the image (not illustrated) is indeed the two boundaries between SCAs. Since the different SCAs can not be inter-calibrated at these high radiance values, we analyze them separately.

Figure 6 shows wavelet energy spectra based on the 2D Haar transform in Eq. (1) and Fig. 1 for the three SCAs. Over these scales (5 m to 1.3 km), we expected a very smooth radiance field due to the horizontal transport of photons across many pixel scales via multiple scattering. This "radiative smoothing" has been quantified by Marshak et al. (1995) and others. We therefore anticipate H to be quite close to unity. This makes the scale-break in Fig. 6 around 2^2 pixels (20 m) rather intriguing. We find the expected H value at larger scales and a negative H, characteristic of stationary noise, at smaller scales. The turn-around in wavelet energy occurs where signal equals noise. Note that, in this study, "signal" means the diminutive wavelet coefficients for a smooth field, not the overall photon counts, while "noise" (whatever its instrumental source may be) is amplified by taking differences of large quantities to compute the wavelet coefficient.

The origin of this detector noise is not fully understood. It is believed to be traceable to the extrapolation of radiometric calibration data gathered for relatively dark targets to the unusually bright —and indeed inadvertent— target in this cloudy image.

We recommend that in cloud studies using MTI data the bright reflected radiances be averaged over scales of at least 4 pixels (in each direction) to obtain noise-free increment metrics such as wavelet coefficients. This brings its effective resolution close to that of LANDSAT (30 m pixels). Contrary to LANDSAT's to saturate at a DN value of 255, MTI's broader dynamic range and 12-bit digitization avoid this pitfall.

FIGURE 6 here

Figure 6: *Second-order spatial statistics for MTI cloud data.* Wavelet analysis of the x-variability is performed for SCA 1 (solid line), SCA 2 (dotted line), SCA 3 (dashed line). The other 2D wavelets illustrated in Fig. 1 give similar results.

Summary

Discriminating between stationary and nonstationary behavior is a non-trivial yet essential task in data analysis in the presence of spatial correlations. Indeed, only the averages of stationary quantities are robust. For instance, geophysical signals from turbulent systems such as clouds are nonstationary; increments however are often stationary in this case over a large range of scales. We have argued that wavelet transforms, especially in their semi-discrete incarnation with a cunningly non-standard normalization convention, lead to improvements over Fourier- and structure-function analyses in this key task.

We have analyzed ground-based/active and satellite/passive remote sensing data on stratus cloud layers with semi-discrete wavelet transforms. For simplicity, the piece-wise constant Haar wavelet was used in the 1D analysis of mm-radar transects, and its extension to 2D by tensor products for the satellite imagery. We confirmed the existence of well-known scaling laws and a lesser-known scale-break that terminates the long-range correlations in cloud structure at a few tens of kilometers.

Our most interesting finding is that scale-breaks in wavelet energy spectra can also be used to diagnose problems in the data, unsuspected artifacts. In this study alone, we found a deficit in variance (traceable to human intervention) in MMCR data and an excess of variance (traceable to an instrumental noise) in MTI data. In the former case, we conjure up situations of direct relevance to the ARM Program were very misleading conclusions can be drawn from seemingly natural comparisons between models or other sources of data. Our recommendation to avoid these pitfalls is to archive MMCR data without interpolation, or to increase the sampling as needed.
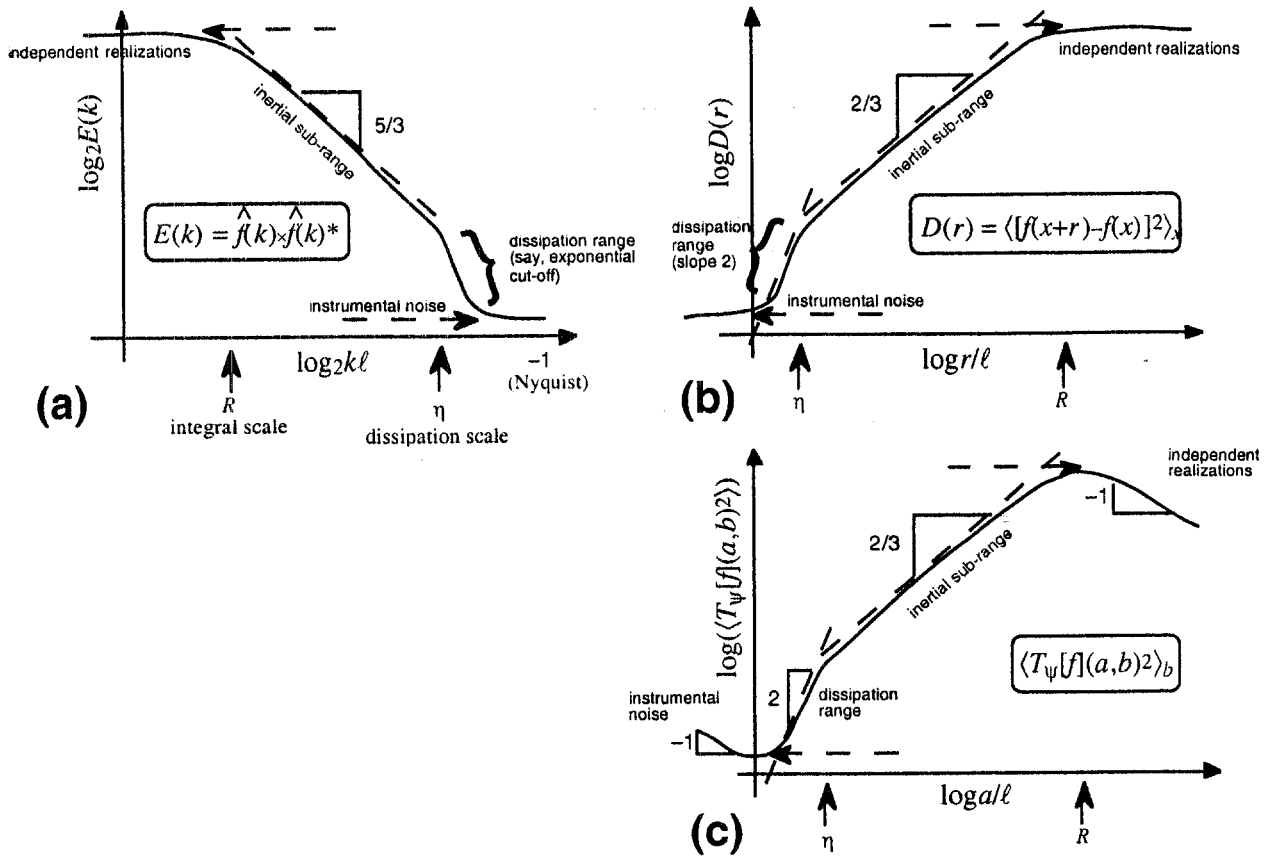
References

Arnéodo, A., E. Bacry, and J.-F. Muzy, 1995: The thermodynamics of fractals revisited with wavelets, *Physica A*, **213**, 232-275.

Austin, P. H., M. Szszodorak, and G. Lewis, 1999: Spatial variability of satellite-retrieved optical depth and effective radius in marine stratocumulus clouds, in *Proceedings of 10th AMS Conference on Atmospheric Radiation*, pp. 237-240, June 28 - July 2, 1999, Madison (Wi), Am. Met. Soc., Boston (Ma).

Clothiaux, E. E., M. A. Miller, B. A. Albrecht, T. P. Ackerman, J. Verlinde, D. M. Babb, R. M. Peters, and W. J. Syrett, 1995: An evaluation of a 94-GHz radar for remote sensing of cloud properties, *J. Atmos. and Oceanic Technol.*, **12**, 201-229.

Daubechies, I., 1992: *Ten Lectures on Wavelets*, x+357 pp, Society of Industrial and Applied Mathematics (SIAM), Philadelphia (Pa).

Davis, A., A. Marshak, R. F. Cahalan, and W. J. Wiscombe, 1997: The LANDSAT scale-break in stratocumulus as a three-dimensional radiative transfer effect, Implications for cloud remote sensing, *J. Atmos. Sci.*, **54**, 241-260.

Davis, A. B., A. Marshak, and E. Clothiaux, 1999: Anisotropic multi-resolution analysis in 2D, Application to long-range correlations in cloud mm-radar fields, in *S.P.I.E. Proceedings, Vol. 3723: Wavelet Applications VI*, Ed. H. H. Szu, pp. 194-207, S.P.I.E., Bellingham (Wa).

Mallat, S., 1989: A theory for multiresolution signal decomposition: The wavelet representation, *IEEE Trans. Pattern Anal. Mach. Intel.*, **11**, 674-693.

Mandelbrot, B. B., 1982: *The Fractal Geometry of Nature*, 460 pp., W. H. Freeman, San Fransisco (Ca).

Marshak, A., A. Davis, W. J. Wiscombe, and R. F. Cahalan, 1995: Radiative smoothing in fractal clouds, *J. Geophys. Res.*, **100**, 26247-26261.

Savigny, C., A. B. Davis, O. Funk, and K. Pfeilsticker, 2002: Time-series of zenith radiance and surface flux under cloudy skies: Radiative smoothing, optical thickness retrievals and large-scale stationarity, *Geophys. Res. Lett.* (in press).

Weber, P. G., B. C. Brock, A. J. Garrett, B. W. Smith, C. C. Borel, W. B. Clodius, S. C. Bender, R. Rex Kay, and M. L. Decker, 1999: Multispectral Thermal Imager mission overview, in *S.P.I.E. Proceedings, vol. 3753: Imaging Spectrometryl V*, eds. M. R. Descour and S. S. Shen, pp. 340-346.
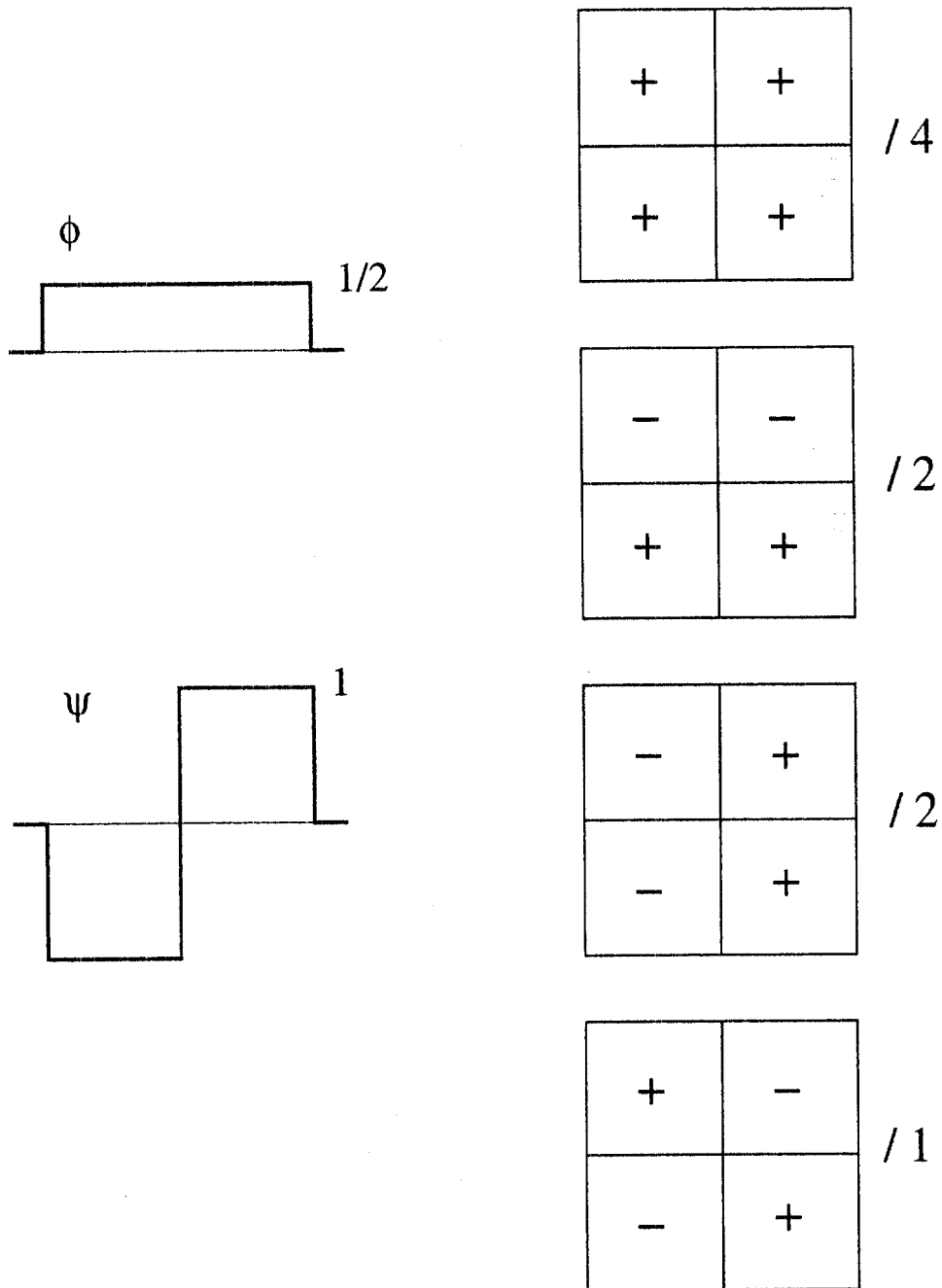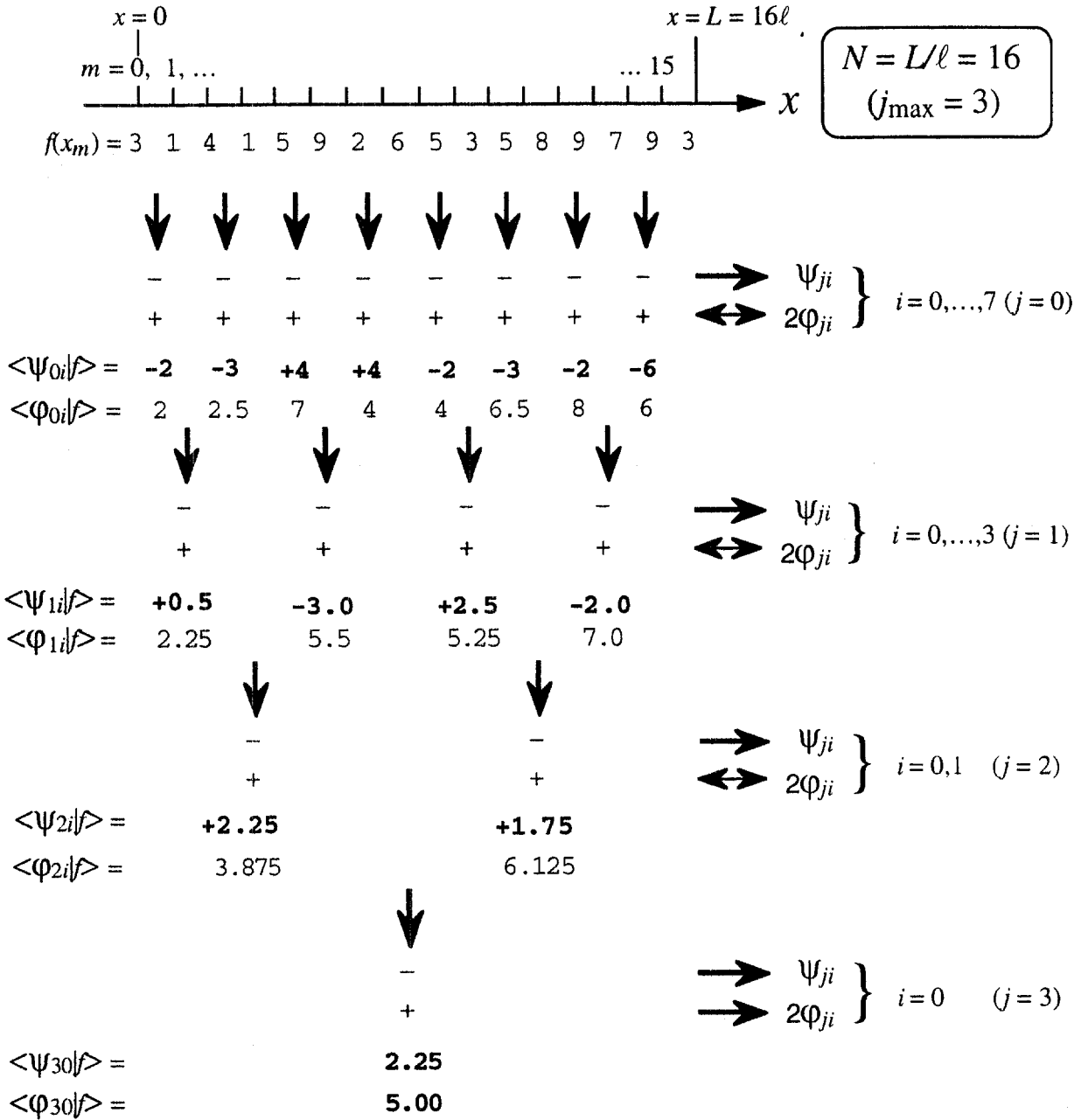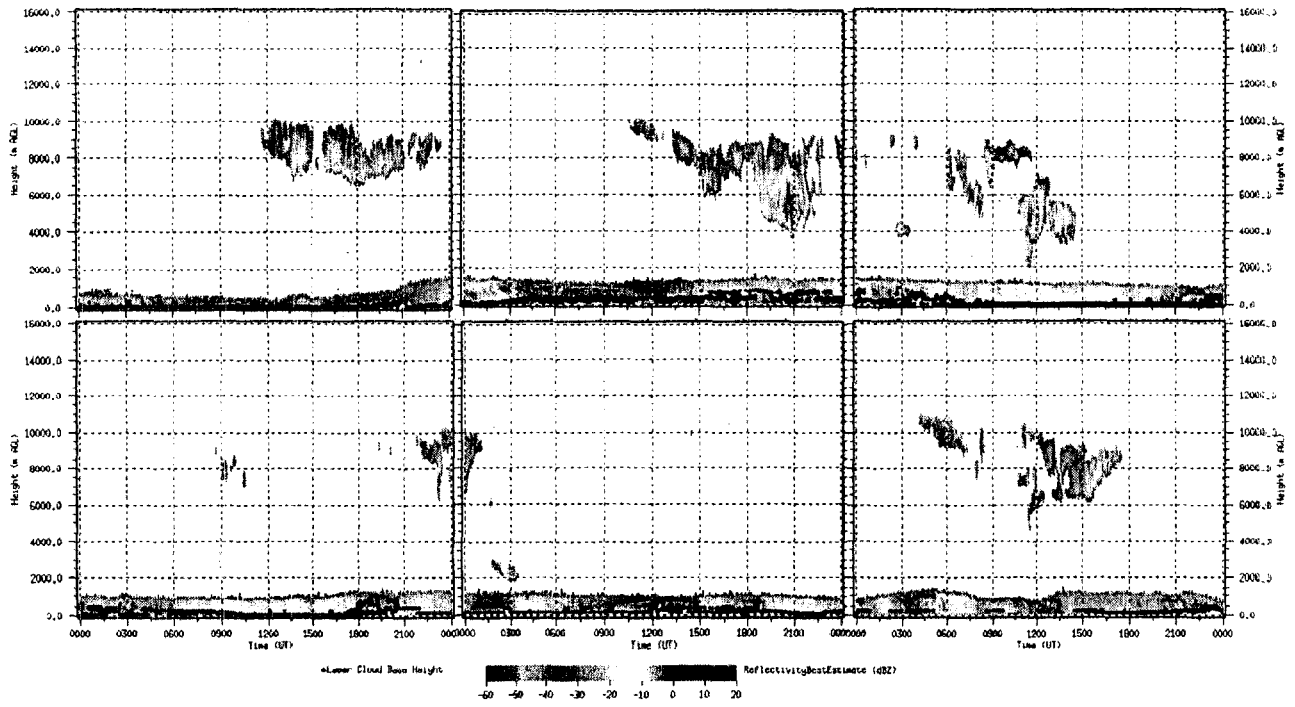
Figure 1: *Haar wavelets and scaling functions in 1D* (left) *and in 2D* (right). The top row are the scaling functions, followed by the characteristically piece-wise constant wavelets.

Figure 2: *Variability analysis in an idealized turbulence experiment.* The "integral" scale R marks the transition from the inertial sub-range, where presumably a down-scale Kolmogorov cascade is unfolding, to an independent cascade. The Kolmogorov or "dissipation" scale η marks the transition from inertial- to dissipation-dominated dynamics. We assume here that the sampling is such that instrumental (e.g., velocity probe) noise dominates the smallest scales, hence a final scale break without any physical significance. **(a)** Fourier spectrum. **(b)** Structure functions. **(c)** Wavelet variance/energy spectrum.

$x = 0$ $x = L = 16\ell$

$m = 0, 1, ...$ ... 15

$\boxed{\begin{array}{c} N = L/\ell = 16 \\ (j_{max} = 3) \end{array}}$

x

$f(x_m) = 3 \quad 1 \quad 4 \quad 1 \quad 5 \quad 9 \quad 2 \quad 6 \quad 5 \quad 3 \quad 5 \quad 8 \quad 9 \quad 7 \quad 9 \quad 3$

ψ_{ji}
$2\varphi_{ji}$ $\Big\}$ $i = 0,...,7 \ (j = 0)$

$\langle\psi_{0i}|f\rangle = \quad -2 \quad\ -3 \quad\ +4 \quad\ +4 \quad\ -2 \quad\ -3 \quad\ -2 \quad\ -6$
$\langle\varphi_{0i}|f\rangle = \quad\ 2 \quad 2.5 \quad\ 7 \quad\quad 4 \quad\quad 4 \quad 6.5 \quad\ 8 \quad\quad 6$

ψ_{ji}
$2\varphi_{ji}$ $\Big\}$ $i = 0,...,3 \ (j = 1)$

$\langle\psi_{1i}|f\rangle = \quad +0.5 \quad\quad -3.0 \quad\quad +2.5 \quad\quad -2.0$
$\langle\varphi_{1i}|f\rangle = \quad 2.25 \quad\quad\ 5.5 \quad\quad\ 5.25 \quad\quad\ 7.0$

ψ_{ji}
$2\varphi_{ji}$ $\Big\}$ $i = 0,1 \quad (j = 2)$

$\langle\psi_{2i}|f\rangle = \quad\quad +2.25 \quad\quad\quad\quad +1.75$
$\langle\varphi_{2i}|f\rangle = \quad\quad\ 3.875 \quad\quad\quad\quad 6.125$

ψ_{ji}
$2\varphi_{ji}$ $\Big\}$ $i = 0 \quad (j = 3)$

$\langle\psi_{30}|f\rangle = \quad\quad\quad 2.25$
$\langle\varphi_{30}|f\rangle = \quad\quad\quad 5.00$
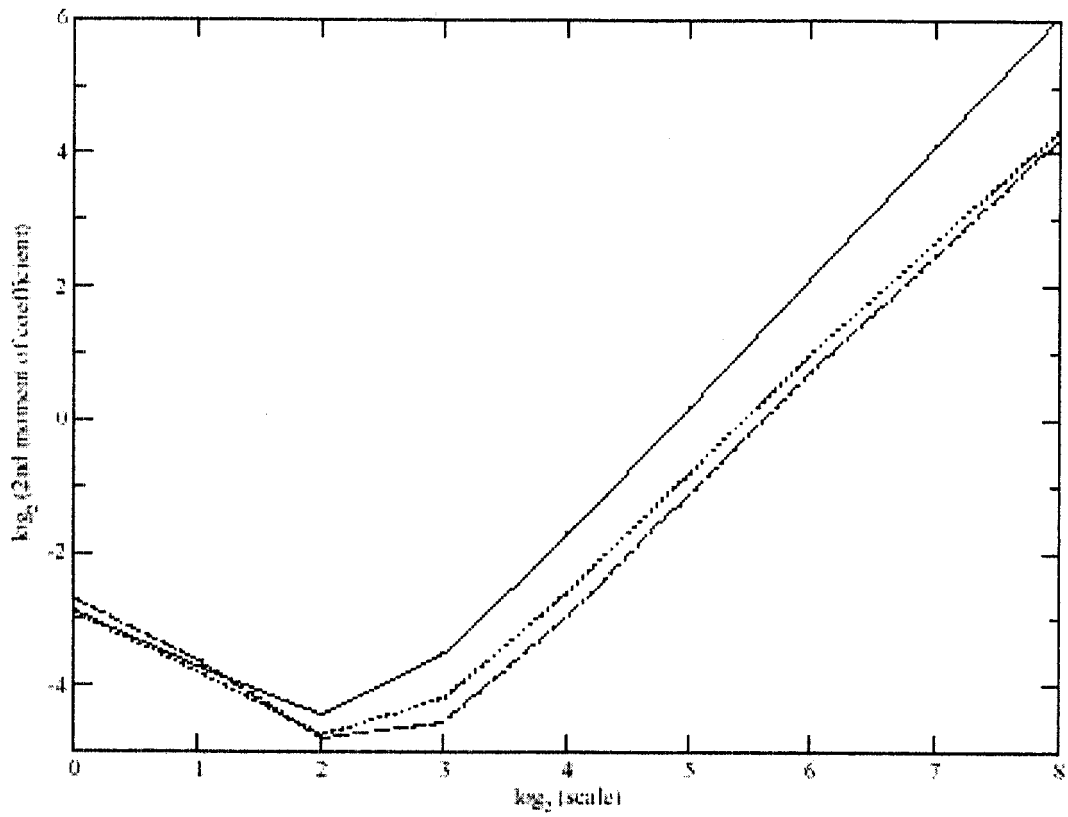
Figure 3: *Discrete Haar wavelet analysis in 1D using multi-resolution analysis for N = 16.* The alternate notation $\langle\psi_{a,b},f\rangle$ for $T_\psi[f](a,b)$ in Eq. (1) is used here where $\psi_{a,b}(x) = \psi((x-b)/a)$. At each step in the (inverse) cascade, *disjoint* 2-pixel averages are computed, yielding the scaling-function coefficients. They are only used to proceed to the next (larger) scale. In the semi-discrete wavelet transform, the only difference is that the 2-pixel averages are not disjoint but, on the contrary, sampled continuously (i.e., at the smallest pixel scale ℓ).

Figure 4: *MMCR data from the SGP site for January 9–14, 1998.* The standard (Clothiaux et al. 1995) rendering of "best-estimate" radar reflectivity is used along with the cielometer-based lower cloud boundary. Time increases day-by-day from left to right, then top to bottom.

Figure 5: *1D semi-discrete wavelet spectrum analysis of horizontal layers of ARM cloud-radar data in Fig. 4.* Solid line: z =180 m; dashed line: z = 630 m.

Figure 6: *Second-order spatial statistics for MTI cloud data.* Wavelet analysis of the x-variability is performed for SCA 1 (solid line), SCA 2 (dotted line), SCA 3 (dashed line). The other 2D wavelets illustrated in Fig. 1 give similar results.